



Cite this: *J. Mater. Chem. A*, 2023, 11, 13275

Rational design of metal–organic frameworks featuring macrocycle and helical chain motifs for propylene/propane separation†

Xinyu Yu, Xin Huang, Mengchu Feng, Yuanyuan Zhang * and Bo Wang *

The separation of propylene/propane is a critical process in the petrochemical industry, and the rational design of porous adsorbents is essential for efficient separation techniques. Designing metal–organic frameworks (MOFs) with supramolecular motifs could access novel structures with finely tuned pore sizes and shapes, opening up new possibilities for enhancing separation performance. Here we report the design and synthesis of three MOF structures, namely BIT-23, 24, and 25, based on a Y-shaped flexible ligand with transition metal nodes (Ni, Zn, or Cu), featuring macrocycle and helical chain motifs. Originating from the flexibility of the ligand and varying geometry of the metal nodes, the formed macrocycle or helical chain units present different conformations, leading to MOFs with distinct topologies and channels. Notably, BIT-23, possessing 1D channels with a periodic structure of wide cavities and narrow bottlenecks and an optimal pore size, could separate propylene/propane, as verified by dynamic breakthrough experiments. The kinetic separation mechanism was further validated by molecular dynamics (MD) simulations.

Received 31st March 2023

Accepted 22nd May 2023

DOI: 10.1039/d3ta01930f

rsc.li/materials-a

Introduction

Propylene (C_3H_6) is one of the most crucial olefins in the petrochemical industry, mainly recovered from cracking processes, in which propane (C_3H_8) is often generated as a byproduct.^{1,2} The efficient separation of C_3H_6/C_3H_8 to produce high-purity C_3H_6 is important for further utilization such as polymer production.^{3,4} However, owing to their similar size and properties, traditional separation techniques, such as cryogenic distillation, demand high energy consumption and operational costs.^{5–7} Adsorptive separation using porous materials presents a high-efficiency and low-capital alternative.^{8,9} Metal–organic frameworks (MOFs), constructed from metal ions or clusters coordinated with organic linkers, are a unique class of porous crystalline material characterized by high porosity and well-defined open channels.^{10–14} The structural diversity, rich functionalities, and finely tuneable channels of MOFs make them promising candidates for C_3H_6/C_3H_8 separation.^{15–20} Kinetic separation relies on the varying transport rate of gas pairs into

an adsorbent, which is particularly effective when separating molecules of similar sizes and polarities, as in the case of C_3H_6 and C_3H_8 . Kinetic separation features high energy efficiency compared to equilibrium separation, as the regeneration process is facilitated due to the absence of strong interactions, making it industrially advantageous. In addition, kinetic separation can also avoid undesirable olefin polymerization, which may occur on open metal sites when heating is utilized to accelerate regeneration.^{21,22} Given the similar dimensions of C_3H_6 and C_3H_8 , fine tuning of the size and shape of MOF channels is important to achieve kinetic separation, albeit it remains a challenging task.^{22,23}

Supramolecular coordination complexes (SCCs) share similar design principles and synthetic approaches to MOFs. Numerous supramolecular cycles, helical chains, and cages with well-defined geometries and sizes have been constructed by a coordination-driven self-assembly approach.^{24–30} These discrete molecular systems feature characteristic cavities or channels, varied connectivity, and flexible geometries, rendering them attractive units for constructing MOFs.^{31–34} Importantly, the shape and size of the framework channels could be fine tuned by adjusting the conformation and spatial arrangement of the supramolecular motifs.^{35–39} A representative example is the supramolecular building blocks (SBBs) approach, which utilizes metal–organic polyhedrons (MOPs) as building entities to construct MOFs, offering an effective way to develop frameworks for gas separation.^{40–42} Inspired by the intriguing properties of SCCs, we aim to design MOFs with supramolecular motifs such as macrocycles and helical chains

Frontiers Science Center for High Energy Material, Key Laboratory of Cluster Science, Ministry of Education, Beijing Key Laboratory of Photoelectronic/Electrophotonic Conversion Materials, Advanced Research Institute of Multidisciplinary Science, Advanced Technology Research Institute (Jinan), School of Chemistry and Chemical Engineering, Beijing Institute of Technology, No. 5, South Street, Zhongguancun, Haidian District, Beijing 100081, China. E-mail: yuanyuan.zhang@bit.edu.cn; bowang@bit.edu.cn

† Electronic supplementary information (ESI) available. CCDC 2174117–2174119. For ESI and crystallographic data in CIF or other electronic format see DOI: <https://doi.org/10.1039/d3ta01930f>

for C₃H₆/C₃H₈ separation, in which the flexible configuration and arrangement of these motifs enable precise tuning of pore size and shape.

Herein, we rationally designed and synthesized three MOFs (denoted BIT-23, BIT-24, and BIT-25, BIT = Beijing Institute of Technology) featuring metal–organic macrocycle or helical chain motifs, using flexible multidentate organic ligands with a bent geometry and transition metal ions (Ni²⁺, Zn²⁺, or Cu²⁺) (Fig. 1). It is known that in the SCC system bent ligands bearing two terminal coordination sites (*i.e.* a V-shaped geometry) could favour the formation of macrocycles and helical chains.^{34,43} To further construct extended structures, we employed a Y-shaped ligand with a third N-coordination site from an imidazole moiety that could offer the opportunity to link the macrocycles or helical chains. In this way, new MOF structures with periodically arranged macrocycles or helical chains were afforded, possessing one-dimensional (1D) channels. Moreover, by altering the metal nodes and their coordination modes, we precisely adjusted the twisting angle of the organic ligand to control the size and geometry of the pore channel in the frameworks. In particular, BIT-23 with 1D channels featuring a periodic structure of wide cavities and narrow bottlenecks and an optimal size realized kinetic separation for propylene/propane, and the separation capability was demonstrated by dynamic breakthrough measurements. The diffusion behaviours of the gases in the 1D channels were studied by molecular dynamics (MD) simulation.

Results and discussion

Structural analysis of BIT-MOFs

All three MOFs were synthesized using the same organic ligand, 4,4'-(1*H*,1'*H*-[2,2'-biimidazole]-1,1'-diyl) dibenzoic acid (H₂BDA), with nickel(II), copper(II), or zinc(II) salts at 120 °C in DMF containing different amounts of ammonia. The structures of BIT-23(Ni), BIT-24(Zn), and BIT-25(Cu) were analyzed by single-crystal X-ray diffraction, and the crystallographic data are

summarized in Tables S2–S8.† It is shown that BIT-23 and BIT-24 are composed of metal–organic macrocycles linked by coordination bonds forming 2D extended structures with 1D channels, and BIT-25 is constructed from helical chains that are further connected to construct 3D networks with 1D channels. These distinct structures are attributed to the differences in geometries of the metal nodes and the ligand, as illustrated in Fig. 2. Specifically, BIT-23 is obtained as pale green lamellar crystals and it crystallizes in the monoclinic system with the *P*₂₁/*c* space group, with a formula of {[Ni(BDA)(NH₃)(H₂O)]·DMF}_{*n*} (Fig. S1†). The asymmetric unit of the crystal structure includes one Ni(II) ion, one water molecule, one ammonia molecule, one BDA²⁻, and a lattice DMF molecule (Fig. S4a†). Individually, the Ni(II) ion adopts a distorted {NiO₄N₂} octahedral coordination geometry, which is surrounded by three carboxylate oxygen atoms from two distinct BDA²⁻ ligands, one nitrogen donor from the imidazole moiety in the ligand, one coordinated water molecule, and one ammonia molecule (Fig. 2a). Two {NiO₄N₂} octahedrons are linked alternately by two BDA²⁻ ligands to form a macrocycle (Ni₂(BDA)₂) (Fig. 2c), which are further connected by Ni–N bonds to generate a 2D layered structure with diamond-shaped channels along the *a*-axis (9.0 Å × 19.1 Å) (Fig. 2d and S5a†). The framework features a 3,3-connected *fes* topology, where each Ni(II) ion and BDA²⁻ ligand is a 3-connected node (Fig. S6a†).

BIT-24 was prepared with Zn(NO₃)₂·6H₂O under similar conditions, giving stick-shaped crystals (Fig. S2†) with the formula {[Zn(BDA)(H₂O)]·DMF}_{*n*}. Structural analysis reveals that BIT-24 crystallizes in the monoclinic *P*₂₁/*c* space group with *fes* topology (Fig. S6a†), which is the same as BIT-23. Its asymmetric unit contains one Zn(II) ion, one water molecule, one BDA²⁻ ligand, and a lattice DMF molecule (Fig. S4b†). Each Zn(II) ion is bound to two monodentate carboxylate groups from two distinct BDA²⁻ ligands, one nitrogen donor from the imidazole moiety, and one coordinated water molecule forming a {ZnO₃N} tetrahedron (Fig. 2e). The two {ZnO₃N} tetrahedrons are alternately linked with BDA²⁻ to form a Zn₂(BDA)₂

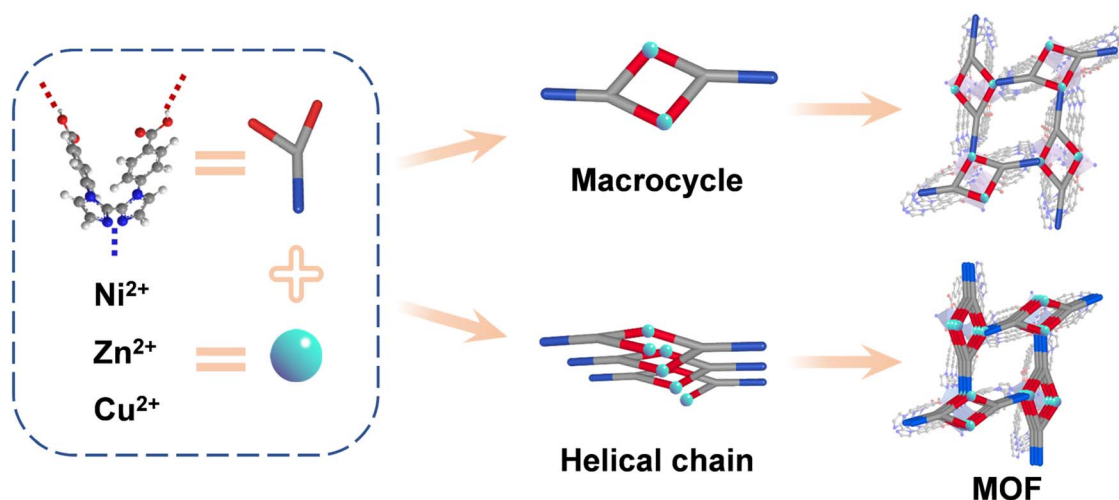


Fig. 1 Schematic illustration of the synthetic strategy for BIT-MOFs.

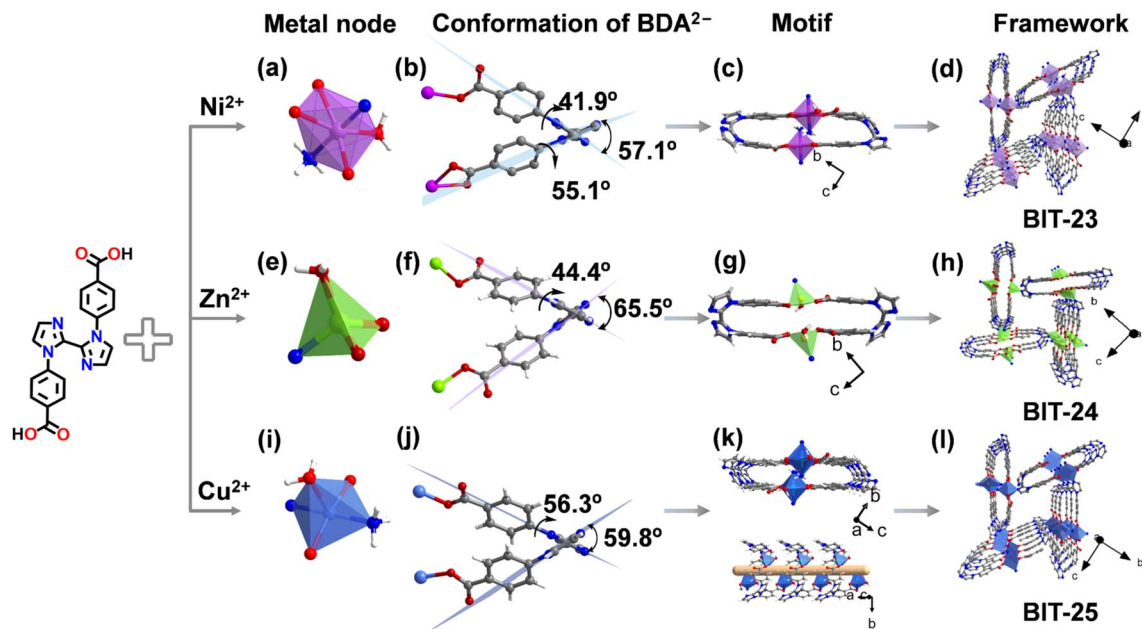


Fig. 2 Crystal structures of BIT-23, BIT-24, and BIT-25 ((d), (h), and (l)) and corresponding metal nodes ((a), (e) and (i)), ligands ((b), (f) and (j)), and supramolecular motifs ((c), (g) and (k)). Atom color scheme: O, red; C, gray; N, blue; H, white; Ni, purple; Zn, green; Cu, light blue; solvent molecules are omitted for clarity.

macrocycle (Fig. 2g). The macrocycle motifs further link with each other *via* Zn–N bonds to form a 2D extended structure with a square-shaped channel of 13.6 Å × 13.8 Å (Fig. 2h and S5b[†]).

Combining Cu(NO₃)₂·3H₂O and H₂BDA in DMF with ammonia, we obtained blue stick-shaped crystals of BIT-25 (Fig. S3[†]) with the formula {[Cu(BDA)(NH₃)(H₂O)]·DMF}_n. It crystallizes in the *P*2₁2₁2₁ space group with an asymmetric unit consisting of one Cu(II) ion, one water molecule, one ammonia molecule, one BDA²⁻, and a lattice DMF molecule (Fig. S4c[†]). Each Cu(II) ion adopts a {CuO₃N₂} quadrangular pyramid geometry, coordinating to two carboxyl oxygen atoms of two distinct ligands, one nitrogen donor from the imidazole moiety, one coordinated water molecule, and an ammonia molecule (Fig. 2i). The BDA²⁻ ligand connects the Cu metal nodes forming a helical chain that intertwines with itself along the *a*-axis, forming a pseudodinuclear Cu₂(BDA)₂ metallomacrocycle when viewed from the top (Fig. 2k). The helical chains are further connected by Cu–N coordination bonds, affording a 3D framework with 1D diamond-shaped channels (14.5 Å × 17.8 Å) (Fig. 2l and S5c[†]), displaying *srs* topology (Fig. S6b[†]).

While the BIT-MOFs are all formed by 3-connected metal nodes and 3-connected BDA²⁻ ligands, they demonstrate different channel shapes or topologies, derived from the variations in metal node geometries as well as the ligand configurations. Due to the different coordination environments of metal ions, the geometries of the corresponding triangular nodes vary. Further analysis of the ligand conformation reveals that the dihedral angles between the two imidazole rings, as well as the twisting angles of the benzoate arms with respect to the connected imidazole ring, differ in these structures (Fig. 2b, f, and j). Specifically, the dihedral angle between the two

imidazole rings in BIT-24 is 65.5°, which is larger than those in BIT-23 and BIT-25 (57.1° and 59.8°, respectively), and correspondingly the channel in BIT-24 is also the largest with a square shape. The benzoate arms exhibit the most severe distortion in BIT-25, with a twisting angle of 56.3°. In comparison, BIT-23 and BIT-24 have twisting angles of 41.9° and 44.4°, respectively. In addition, the distance between the two metal nodes linked by a single BDA²⁻ ligand in BIT-25 is also the closest, measuring 3.3 Å along the direction of the 1D channel and 3.6 Å in the direction perpendicular to it (Fig. S7 and S8[†]). These factors possibly contribute to the unique topology in BIT-25, distinguishing it from the other two structures.

Characterization

The phase purity of BIT-23, BIT-24, and BIT-25 was verified by powder X-ray diffraction (PXRD) (Fig. 3a), and the experimental diffraction patterns match well with the simulated ones. After activation, the morphology of the BIT-MOFs crystals was maintained, as shown in the scanning electron microscopy (SEM) images (Fig. S9[†]). In the IR spectra of the activated BIT-MOFs, a noticeable red-shift in the C=O stretching vibration peak confirms that carboxyl groups in H₂BDA are coordinated with metal ions (Fig. S10[†]). Thermogravimetric analyses (TGA) indicate that activated BIT-23 and BIT-24 show weight losses resulting from structural decomposition at 325 °C and 350 °C, respectively, while a small amount of weight loss at lower temperatures might be attributed to the presence of lattice DMF (Fig. S11[†]). For activated BIT-25, the weight loss observed between 80 and 220 °C is due to the coordinated water and ammonia molecules, and structural decomposition occurs at

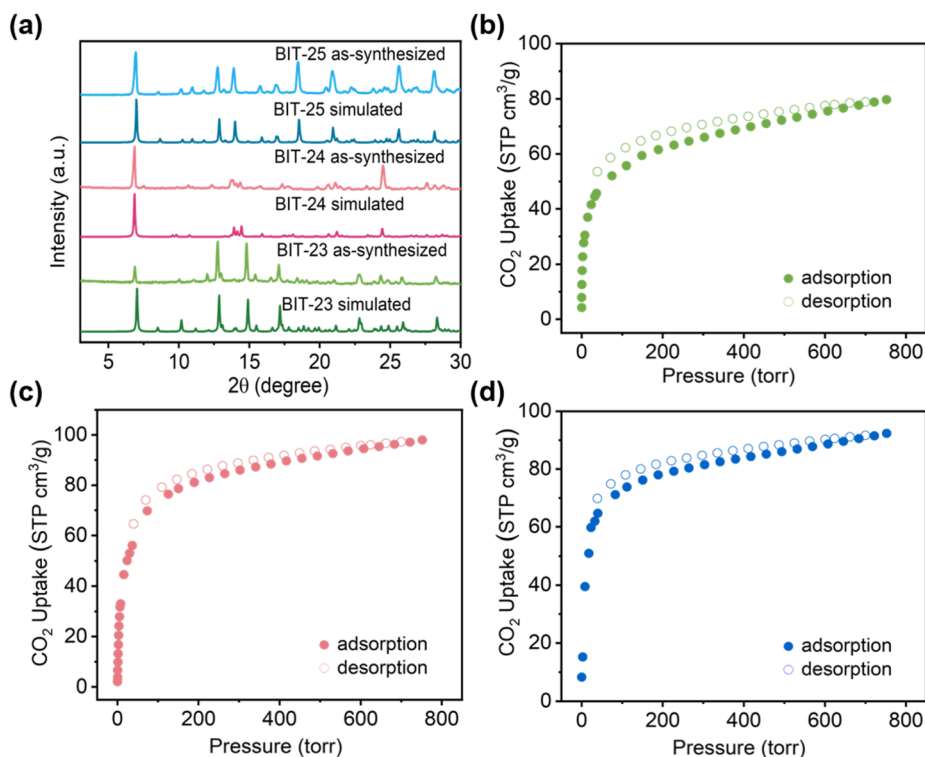


Fig. 3 Characterization of BIT-MOFs. (a) PXRD patterns of BIT-23, BIT-24, and BIT-25. CO₂ sorption isotherms of (b) BIT-23, (c) BIT-24, and (d) BIT-25 at 195 K.

260 °C. Elemental analysis results confirm the residual DMF, water, and ammonia molecules (Table S1†). Given the ultramicropores observed in the crystal structure of BIT-MOFs, the permanent porosity of BIT-MOFs was evaluated by CO₂ sorption measured at 195 K, presenting a type I isotherm (Fig. 3b–d). The BET surface areas for BIT-23, BIT-24, and BIT-25 are calculated to be 402, 461, and 549 m² g⁻¹, respectively. The pore size distribution based on the carbon non-local density functional theory (NLDFT) model shows main peaks at 4.6, 5.3, and 4.8 Å for BIT-23, BIT-24, and BIT-25, respectively (Fig. S12–14†). Furthermore, the chemical stability of BIT-MOFs was tested by soaking them in various solutions, including water, acidic aqueous solution (HCl), alkaline aqueous solution (NaOH), and organic solvents (MeOH and CH₂Cl₂) for 12 h, respectively. The crystallinity and porosity of the MOFs are all maintained, as evidenced by the PXRD patterns and CO₂ sorption isotherms (Fig. S15–17†), suggesting their high chemical stability. To assess the thermal stability, we collected the PXRD data of the BIT-MOFs after heating under an N₂ atmosphere. It is seen that activated BIT-23, BIT-24, and BIT-25 maintain their structures up to 295 °C, 305 °C, and 210 °C, respectively (Fig. S18†).

Propylene/propane separation performance

Taking advantage of the tunable geometry of the metal nodes and linker, the shape and dimension of the pore channels in BIT-MOFs could be fine tuned, making them promising candidates as adsorbents for gas separation. The adsorption and separation performances of C₃H₆ and C₃H₈ were estimated

for BIT-MOFs in view of their highly porous structures with ultramicropores. The time-dependent kinetic adsorption of C₃H₆ and C₃H₈ for BIT-MOFs was measured at 298 K and 1 bar (Fig. 4a and S19†). BIT-23 showed faster uptake for C₃H₆ than for C₃H₈, while BIT-24 and BIT-25 present no significant differences for the two gases, suggesting that BIT-23 has a kinetic selectivity for C₃H₆ over C₃H₈. To quantify the kinetic selectivity, the diffusional time constants ($D' = D_c/r_c^2$, where D_c is the intracrystalline diffusivity of gas molecules in porous media and r_c is the radius of the equivalent spherical particle) for the two gases were calculated,^{22,44,45} and the kinetic selectivities of BIT-23, BIT-24, and BIT-25 ($D'(C_3H_6)/D'(C_3H_8)$) were calculated to be 9.06, 1.39, and 2.70 at 298 K, respectively (Fig. S20 and 21†). Single-component sorption isotherms of C₃H₆ and C₃H₈ for BIT-MOFs were collected at 288 K, 298 K, and 303 K (Fig. 5b and S22–24†). The equilibrium uptakes of C₃H₆ and C₃H₈ were close for BIT-23, with capacities of 1.5 mmol g⁻¹ and 1.4 mmol g⁻¹, respectively, at 298 K and 1 bar, and the derived isosteric heats of adsorption (Q_{st}) suggest similar affinity for the two gases (Fig. S25†). Similarly, BIT-24 and BIT-25 did not show obvious thermodynamic selectivity for C₃H₆/C₃H₈. These findings suggest that BIT-23 could provide optimal channels for realizing kinetic sieving of C₃H₆ and C₃H₈.

To evaluate the separation capability of BIT-23 for a mixed gas, column breakthrough experiments were performed with a binary mixture of C₃H₆/C₃H₈ in a 50/50 (v/v) ratio. Breakthrough curves show that C₃H₈ eluted out before C₃H₆, and the dynamic adsorption uptakes of C₃H₈ and C₃H₆ were calculated

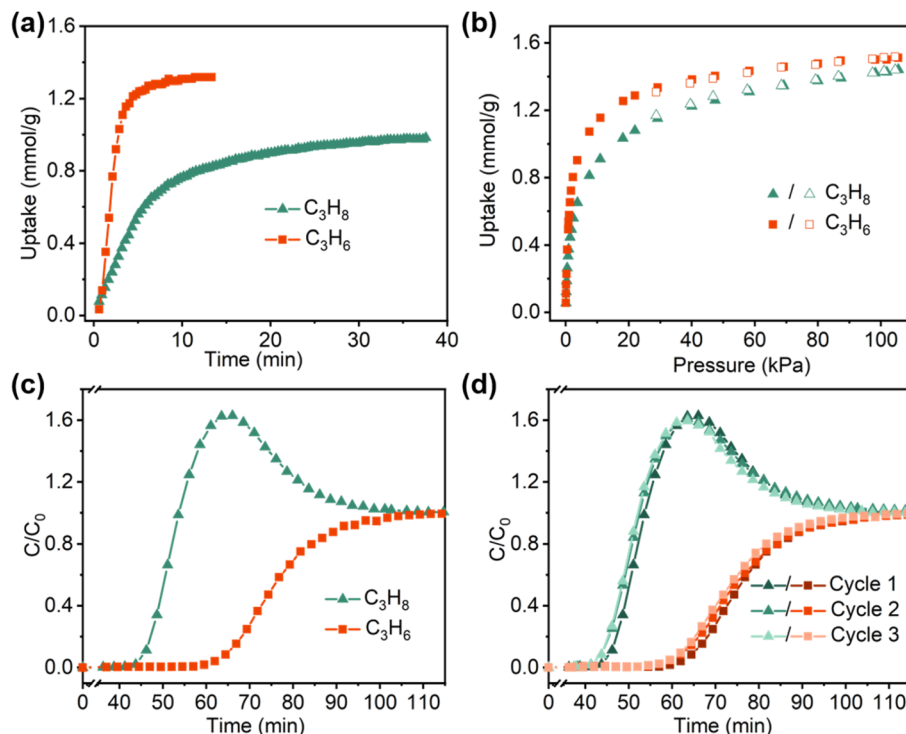


Fig. 4 The gas adsorption and separation properties of BIT-23. (a) Kinetic adsorption profiles of C_3H_6 and C_3H_8 for BIT-23 at 298 K and 1 bar. (b) Single-component sorption isotherms of propane and propylene on BIT-23 at 298 K. (c) Dynamic breakthrough curves of BIT-23 for C_3H_8/C_3H_6 (50/50, v/v) at 298 K and 1 bar. (d) Breakthrough curves of BIT-23 for C_3H_8/C_3H_6 over three cycles.

to be 0.39 mmol g^{-1} and 0.86 mmol g^{-1} , respectively, giving a separation factor of 2.2 (Fig. 4c and S26[†]). Desorption experiments on BIT-23 were conducted to determine the productivity for C_3H_6 . It is estimated that 0.29 mmol g^{-1} of C_3H_6 with 94% purity can be recovered in a single cycle (Fig. S27[†]). As for BIT-24 and BIT-25, the breakthrough times for C_3H_6 and C_3H_8 were close under the same experimental conditions (Fig. S28 and 29[†]). Through three runs of dynamic breakthrough experiments (Fig. 4d), it is verified that BIT-23 can be regenerated, and repeated activation and utilization will not significantly affect

the dynamic selectivity or adsorption capacity of the material. Meanwhile, the PXRD patterns and IR spectra of recycled BIT-23 coincided well with those of the initially activated samples, demonstrating that BIT-23 presents good stability during the cyclical regenerative process (Fig. S30[†]).

MD simulations

The Connolly surface of BIT-23 revealed that the 1D channels are composed of larger cavities interconnected by narrow bottlenecks in a periodic manner (Fig. 5 and S31[†]). The

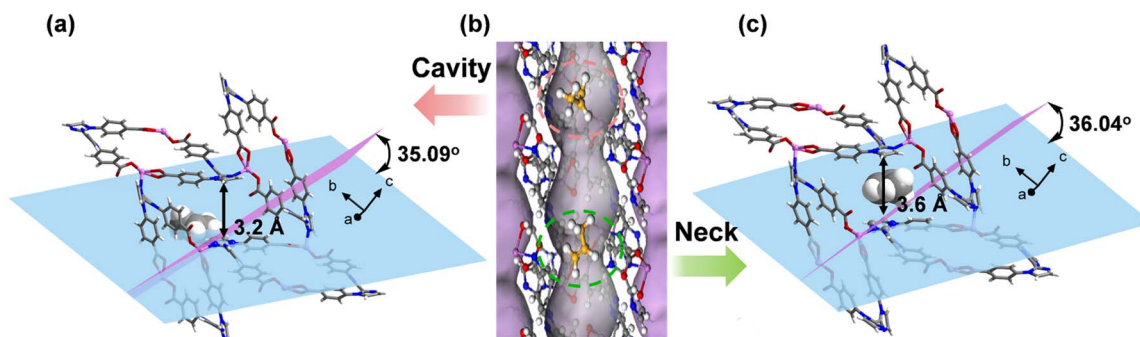


Fig. 5 (a) MD simulated snapshot of the large cavity in BIT-23 with a C_3H_6 molecule (depicted in space-filling mode). (b) Connolly surface of BIT-23 with C_3H_6 molecules in the channel. C_3H_6 is depicted in ball-stick mode with orange carbon atoms. (c) MD simulated snapshot of the bottleneck in BIT-23 with a C_3H_6 molecule (depicted in space-filling mode). The narrowest distances of the bottleneck structure in (a) and (c) are 3.2 and 3.6 Å, respectively. Color code: O, red; C, gray; N, blue; H, white; Ni, purple; the plane of the imidazole ring, grayish blue; the plane formed by linking four Ni(II) ions in two macrocycles along the *a*-axis direction, pink.

narrowest distance of the bottleneck structure is determined by the distance between the two carbon atoms from two imidazole groups (Fig. S32†). We anticipated that the rotation of the imidazole moiety may dynamically influence the aperture of the neck structure and consequently affect the diffusion of the guest molecules with varying molecular dimensions. To gain a deeper insight into the separation mechanism of BIT-23, we performed MD simulations to investigate the diffusion behaviours of C_3H_6 and C_3H_8 in the 1D channels. As shown in the MD simulated snapshots (Fig. 5a and c), when C_3H_6 molecules were introduced, the imidazole moiety rotated 0.95° (from 35.09° to 36.04°) with respect to the plane formed by linking four Ni(II) ions in two macrocycles along the a -axis, thus expanding the size of the bottleneck window from 3.2 \AA to 3.6 \AA and enabling the passage of C_3H_6 . In contrast, due to the larger molecular size of C_3H_8 , a wider window size of 4.0 \AA is required to enable its diffusion, and the imidazole group needs to rotate by a larger angle of 7° (from 35.68° to 28.68°) (Fig. S33†), implying that C_3H_8 with larger molecular size would require more energy to be transported through the narrow bottleneck of BIT-23.⁴⁶ The kinetic adsorption experimental results also confirmed that the diffusion rate of C_3H_8 was slower than that of C_3H_6 . The poor kinetic separation performance of BIT-24 and BIT-25 could be ascribed to the influence of subtle structural differences. The slight differences in the twist angle of the H_2BDA lead to small but notable changes in motif geometry. Consequently, this results in different effective pore sizes in the frameworks (Fig. S34†). In light of the minimal difference in the kinetic diameters of C_3H_6 and C_3H_8 (0.2 \AA),⁴⁷ a seemingly slight increase in the channel size would have a significant impact on separation capability.

Conclusions

In summary, we designed and synthesized three new MOFs with macrocycle or helical chain motifs, utilizing a Y-shaped ligand and transition metal nodes (Ni, Zn, or Cu). The rational construction and periodic arrangement of the macrocycle or helical chain motifs lead to highly ordered porous frameworks with 1D channels. The flexibility of the ligand and tuneable geometry of the metal nodes allow for the precise regulation of the frameworks together with the channels. Notably, BIT-23, with optimal pore dimension and a structure of cavities interconnected by narrow bottlenecks, shows potential for the separation of propylene/propane, as verified by dynamic breakthrough experiments. The kinetic separation mechanism was further supported by MD simulations. The diversity and complexity of supramolecular coordination motifs offer new opportunities for enriching MOF structures and applications.

Experimental section

Synthesis of BIT-23

In a sealed 20 mL glass vial, $Ni(NO_3)_2 \cdot 6H_2O$ (0.0174 g, 0.06 mmol) and H_2BDA (0.0224 g, 0.06 mmol) were dissolved in DMF (5.5 mL) and $NH_3 \cdot H_2O$ (0.3 mL). After sonication for 3 min, the vial was heated under autogenous pressure in a preheated oven

at $120^\circ C$ for 48 h. After cooling to room temperature, pale green lamellar crystals were obtained.

Synthesis of BIT-24

In a sealed 20 mL glass vial, $Zn(NO_3)_2 \cdot 6H_2O$ (0.0535 g, 0.18 mmol) and H_2BDA (0.0224 g, 0.06 mmol) were dissolved in DMF (5.6 mL) and $NH_3 \cdot H_2O$ (0.4 mL). After sonication for 3 min, the vial was heated under autogenous pressure in a preheated oven at $120^\circ C$ for 48 h. After cooling to room temperature, colorless stick-shaped crystals were obtained.

Synthesis of BIT-25

In a sealed 20 mL glass vial, $Cu(NO_3)_2 \cdot 3H_2O$ (0.0145 g, 0.06 mmol) and H_2BDA (0.0224 g, 0.06 mmol) were dissolved in DMF (7 mL) and $NH_3 \cdot H_2O$ (0.3 mL). After sonication for 3 min, the vial was heated under autogenous pressure in a preheated oven at $120^\circ C$ for 48 h. After cooling to room temperature, blue stick-shaped crystals were obtained.

Author contributions

Xinyu Yu: investigation, materials synthesis, characterization measurements, data curation, writing – original draft. Xin Huang and Mengchu Feng: data curation. Yuanyuan Zhang and Bo Wang: conceptualization, funding acquisition, writing – review & editing.

Conflicts of interest

There are no conflicts to declare.

Acknowledgements

We thank the National Natural Science Foundation of China (Grant No. 22005030, 22271015, 21971017), the National Key Research and Development Program of China (No. 2020YFB1506300), Beijing Institute of Technology Research Fund Program for financial support, and Analysis and Testing Center of Beijing Institute of Technology.

References

- 1 D. Antypov, A. Shkurenko, P. M. Bhatt, Y. Belmabkhout, K. Adil, A. Cadiou, M. Suyetin, M. Eddaoudi, M. J. Rosseinsky and M. S. Dyer, *Nat. Commun.*, 2020, **11**, 6099.
- 2 M. L. Balogun, S. Adamu, I. A. Bakare, M. S. Ba-Shammakh and M. M. Hossain, *J. CO₂ Util.*, 2020, **42**, 101329.
- 3 C. C. E. Christopher, A. Dutta, S. Farooq and I. A. Karimi, *Ind. Eng. Chem. Res.*, 2017, **56**, 14557–14564.
- 4 M. Khalighi, Y. F. Chen, S. Farooq, I. A. Karimi and J. W. Jiang, *Ind. Eng. Chem. Res.*, 2013, **52**, 3877–3892.
- 5 H. Zeng, M. Xie, T. Wang, R. J. Wei, X. J. Xie, Y. Zhao, W. Lu and D. Li, *Nature*, 2021, **595**, 542–548.
- 6 D. S. Sholl and R. P. Lively, *Nature*, 2016, **532**, 435–437.

- 7 H. Jarvelin and J. R. Fair, *Ind. Eng. Chem. Res.*, 1993, **32**, 2201–2207.
- 8 D.-D. Zhou and J.-P. Zhang, *Acc. Chem. Res.*, 2022, **55**, 2966–2977.
- 9 L. Yang, S. Qian, X. Wang, X. Cui, B. Chen and H. Xing, *Chem. Soc. Rev.*, 2020, **49**, 5359–5406.
- 10 H. Furukawa, K. E. Cordova, M. O’Keeffe and O. M. Yaghi, *Science*, 2013, **379**, 330–331.
- 11 R.-B. Lin, Z. Zhang and B. Chen, *Acc. Chem. Res.*, 2021, **54**, 3362–3376.
- 12 H.-Y. Li, S.-N. Zhao, S.-Q. Zang and J. Li, *Chem. Soc. Rev.*, 2020, **49**, 6364–6401.
- 13 G. Cai, P. Yan, L. Zhang, H.-C. Zhou and H.-L. Jiang, *Chem. Rev.*, 2021, **121**, 12278–12326.
- 14 H.-C. J. Zhou and S. Kitagawa, *Chem. Soc. Rev.*, 2014, **43**, 5415–5418.
- 15 X. Zhao, Y. Wang, D.-S. Li, X. Bu and P. Feng, *Adv. Mater.*, 2018, **30**, 1705189.
- 16 S. Zhang, M. K. Taylor, L. Jiang, H. Ren and G. Zhu, *Chem. – Eur. J.*, 2020, **26**, 3205–3221.
- 17 H. Zeng, M. Xie, T. Wang, R.-J. Wei, X.-J. Xie, Y. Zhao, W. Lu and D. Li, *Nature*, 2021, **595**, 542–548.
- 18 Z. Chen, K. O. Kirlikovali, P. Li and O. K. Farha, *Acc. Chem. Res.*, 2022, **55**, 579–591.
- 19 Y. Xie, Y. Shi, E. M. Cedeño Morales, A. El Karch, B. Wang, H. Arman, K. Tan and B. Chen, *J. Am. Chem. Soc.*, 2023, **145**, 2386–2394.
- 20 D. Liu, J. Pei, X. Zhang, X.-W. Gu, H.-M. Wen, B. Chen, G. Qian and B. Li, *Angew. Chem., Int. Ed.*, 2023, **62**, e202218590.
- 21 Y. Wang and D. Zhao, *Cryst. Growth Des.*, 2017, **17**, 2291–2308.
- 22 C. Y. Lee, Y. S. Bae, N. C. Jeong, O. K. Farha, A. A. Sarjeant, C. L. Stern, P. Nickias, R. Q. Snurr, J. T. Hupp and S. T. Nguyen, *J. Am. Chem. Soc.*, 2011, **133**, 5228–5231.
- 23 B. Liang, X. Zhang, Y. Xie, R. B. Lin, R. Krishna, H. Cui, Z. Li, Y. Shi, H. Wu, W. Zhou and B. Chen, *J. Am. Chem. Soc.*, 2020, **142**, 17795–17801.
- 24 S. Datta, M. L. Saha and P. J. Stang, *Acc. Chem. Res.*, 2018, **51**, 2047–2063.
- 25 F. A. Cotton, C. Lin and C. A. Murillo, *Acc. Chem. Res.*, 2001, **34**, 759–771.
- 26 M. D. Pluth and K. N. Raymond, *Chem. Soc. Rev.*, 2007, **36**, 161–171.
- 27 N. C. Gianneschi, M. S. Masar and C. A. Mirkin, *Acc. Chem. Res.*, 2005, **38**, 825–837.
- 28 R. Tabuchi, H. Takezawa and M. Fujita, *Angew. Chem., Int. Ed.*, 2022, **61**, e202208866.
- 29 G.-F. Huo, X. Shi, Q. Tu, Y.-X. Hu, G.-Y. Wu, G.-Q. Yin, X. Li, L. Xu, H.-M. Ding and H.-B. Yang, *J. Am. Chem. Soc.*, 2019, **141**, 16014–16023.
- 30 Y.-H. Kang, X.-D. Liu, N. Yan, Y. Jiang, X.-Q. Liu, L.-B. Sun and J.-R. Li, *J. Am. Chem. Soc.*, 2016, **138**, 6099–6102.
- 31 H. Zhang, R. Zou and Y. Zhao, *Coord. Chem. Rev.*, 2015, **292**, 74–90.
- 32 S. V. Dummert, H. Saini, M. Z. Hussain, K. Yadava, K. Jayaramulu, A. Casini and R. A. Fischer, *Chem. Soc. Rev.*, 2022, **51**, 5175–5213.
- 33 V. Guillerme and M. Eddaoudi, *Acc. Chem. Res.*, 2021, **54**, 3298–3312.
- 34 T. R. Cook, Y. R. Zheng and P. J. Stang, *Chem. Rev.*, 2013, **113**, 734–777.
- 35 Z.-W. Li, X. Wang, L.-Q. Wei, I. Ivanović-Burmazović and G.-F. Liu, *J. Am. Chem. Soc.*, 2020, **142**, 7283–7288.
- 36 S.-T. Zhang, J. Yang, H. Wu, Y.-Y. Liu and J.-F. Ma, *Chem. – Eur. J.*, 2015, **21**, 15806–15819.
- 37 N. Song, T. Kakuta, T.-a. Yamagishi, Y.-W. Yang and T. Ogoshi, *Chem*, 2018, **4**, 2029–2053.
- 38 E. I. Koshevoy, D. G. Samsonenko, A. S. Berezin and V. P. Fedin, *Eur. J. Inorg. Chem.*, 2019, **2019**, 4321–4327.
- 39 A. Cadiau, K. Adil, P. M. Bhatt, Y. Belmabkhout and M. Eddaoudi, *Science*, 2016, **353**, 137–140.
- 40 D.-X. Xue, A. Cadiau, Ł. J. Weseliński, H. Jiang, P. M. Bhatt, A. Shkurenko, L. Wojtas, C. Zhijie, Y. Belmabkhout, K. Adil and M. Eddaoudi, *Chem. Commun.*, 2018, **54**, 6404–6407.
- 41 L. Yu, X. Han, H. Wang, S. Ullah, Q. Xia, W. Li, J. Li, I. da Silva, P. Manuel, S. Rudić, Y. Cheng, S. Yang, T. Thonhauser and J. Li, *J. Am. Chem. Soc.*, 2021, **143**, 19300–19305.
- 42 H. Wang, X. Dong, V. Colombo, Q. Wang, Y. Liu, W. Liu, X.-L. Wang, X.-Y. Huang, D. M. Proserpio, A. Sironi, Y. Han and J. Li, *Adv. Mater.*, 2018, **30**, 1805088.
- 43 W. M. Bloch and G. H. Clever, *Chem. Commun.*, 2017, **53**, 8506–8516.
- 44 Y. Park, D.-K. Moon, D. Park, M. Mofarahi and C.-H. Lee, *Sep. Purif. Technol.*, 2019, **212**, 952–964.
- 45 L. Li, R.-B. Lin, X. Wang, W. Zhou, L. Jia, J. Li and B. Chen, *Chem. Eng. J.*, 2018, **354**, 977–982.
- 46 L. Yang, X. Cui, Y. Zhang, Q. Yang and H. Xing, *J. Mater. Chem. A*, 2018, **6**, 24452–24458.
- 47 K. Li, D. H. Olson, J. Seidel, T. J. Emge, H. Gong, H. Zeng and J. Li, *J. Am. Chem. Soc.*, 2009, **131**, 10368–10369.